

# Opening a new window on MR-based Electrical Properties Tomography with deep learning

Stefano Mandija<sup>1</sup>, Ettore F. Melià<sup>1,2</sup>, Niek R. F. Huttinga<sup>1</sup>,  
Peter R. Luijten<sup>1,3</sup>, Cornelis A. T. van den Berg<sup>1,4</sup>

<sup>1</sup> Center for Image Sciences, University Medical Center Utrecht, Heidelberglaan 100, Utrecht, 3584 CX, The Netherlands.

<sup>2</sup> MR Code BV, Schimminck 18, Zaltbommel, 5301 KR, The Netherlands.

<sup>3</sup> Department of Radiology, University Medical Center Utrecht, Heidelberglaan 100, Utrecht, 3584 CX, The Netherlands.

<sup>4</sup> Department of Radiotherapy, University Medical Center Utrecht, Heidelberglaan 100, Utrecht, 3584 CX, The Netherlands.

In submission to PNAS (<http://www.pnas.org/>)

## Correspondence to:

Mandija Stefano,  
Center for Image Sciences,  
University Medical Center Utrecht,  
Radiology Heidelberglaan 100,  
3584 CX, E01.132, Utrecht,  
The Netherlands  
email: [S.Mandija@umcutrecht.nl](mailto:S.Mandija@umcutrecht.nl)

**Key words:** Conductivity, Permittivity, Electrical Properties, MR-EPT, EPT, Deep Learning, DL-EPT

## Abstract

Electrical properties (EPs) of tissues, conductivity and permittivity, are modulated by the ionic and water content, which change in presence of pathologies. Therefore, information on tissues EPs can be used e.g. as an endogenous biomarker in oncology. MR-Electrical Properties Tomography (MR-EPT) aims to reconstruct tissue EPs by solving an electromagnetic inverse problem relating MR measurements of the transmit radiofrequency (RF) field to the EPs. However, current MR-EPT reconstructions highly suffer from noise in the RF field maps, which limits their clinical applicability. Instead of employing electromagnetic models posing strict requirements on the measured electromagnetic quantities, we propose to use a data driven approach where the inverse transformation is learned by means of a neural network.

Supervised training of a conditional generative adversarial neural network was performed using simulated realistic RF field maps and realistic human head dielectric models. Deep learning EPT (DL-EPT) reconstructions are presented for in-silica MR data and MR measurements at 3 Tesla on phantoms and human brains.

DL-EPT shows high quality EP maps, demonstrating good accuracy and greatly improved precision compared to conventional MR-EPT. Moreover, DL-EPT allows permittivity reconstructions at 3 Tesla, which is not possible with state-of-art MR-EPT techniques. The supervised learning-based approach leverages the strength of tailored electromagnetic simulations, allowing inclusion of a priori information (e.g. coil setup) and circumvention of inaccessible MR electromagnetic quantities. Since DL-EPT is highly noise-robust, the requirements for MRI data acquisitions can be relaxed, allowing faster acquisitions and higher resolutions.

We believe that DL-EPT greatly improves the quality and applicability of EPT opening a new window for an endogenous biomarker in MRI diagnostics that reflects differences in ionic tissue content.

## Significant Statement

The inability of MR-Electrical Properties Tomography (MR-EPT) to accurately reconstruct tissue electrical properties (EPs) severely limits the clinical use of EPs mapping e.g. as a biomarker in oncology. We demonstrate that the EPT reconstruction problem can be casted as a supervised deep learning (DL) task. The presented DL-EPT reconstructions for both in-silica and experimental MR data at 3 Tesla on phantoms and human brains demonstrate a great improvement. This could be a key innovation step to turn EPT into a reliable biomarker revealing information on tissue ionic composition as a surrogate of a different metabolism caused by pathological conditions.

## Introduction

Non-invasive measurements of human tissue Electrical Properties (EPs), namely conductivity  $\sigma$  and relative permittivity  $\epsilon_r$ , is a challenge that attracted several research groups in the past decades (1, 2). These properties determine how electromagnetic (EM) fields, such as the MR radiofrequency fields (RF: 64-300 MHz), interact with human tissues. Tissue EPs depend on the tissue structure and composition (water content and ionic concentration). In particular, tissue conductivity is modulated by the total ionic content, which varies in presence of pathologies. Several studies already showed a change in tissue conductivity in presence of tumors (3–7). Therefore, non-invasive measurements of tissue EPs could in principle be used as a new endogenous biomarker in oncology for diagnostic purposes and treatment monitoring (7).

In the early 1990s, an MR-based technique has been suggested to non-invasively measure tissue EPs at the Larmor frequency (64-300 MHz for clinical MR systems), which depends on the exact MR magnetic field strength (8). However, systematic research only started in the last decade, creating a new branch of research called MR-Electrical Properties Tomography (MR-EPT) (9). First MR-EPT approaches aimed to reconstruct tissue EPs by measuring the RF transmit magnetic field, i.e. the circularly polarized transverse magnetic field referred to as the  $\tilde{B}_1^+$  field. This  $\tilde{B}_1^+$  field consists of incident and scattered field terms, where the latter component includes contributions from conduction and displacement currents and thus contains the desired EPs information. By applying the homogenous Helmholtz equation to the measured  $\tilde{B}_1^+$  field, EPs map can be reconstructed.

According to this analytical reconstruction model, tissue EPs can be obtained by computing second order spatial derivatives of the  $\tilde{B}_1^+$  field (10, 11). Spatial derivatives can be computed by applying a filter (in this case a 2<sup>nd</sup> order finite difference filter) to the  $\tilde{B}_1^+$  field data, resulting directly in EPs maps. However, this operation is highly sensitive to the intrinsic noise in the MR measurements, and consequently the reconstructed EPs maps lack precision (12, 13). In particular, for clinical MRI systems (1.5 and 3 Tesla) permittivity reconstructions are not yet feasible since the electromagnetic imprint of related displacement currents is too low at these frequencies.

Recently, alternative analytical reconstruction techniques have been presented to improve the quality of MR-EPT reconstructions (14–18). However, these techniques typically require complex RF setups (multi-transmit array) and high field MR scanners (7 Tesla) are needed to achieve sufficient signal-to-noise-ratio (SNR).

From a fundamental point of view, these analytical reconstruction techniques are computationally fast but require data with high SNR. Instead, algebraic algorithms, which employ a more general inverse approach using iterative minimization, behave better under noisy conditions. However, this comes at the expense of a higher computational load, challenges related to local minima, more complex electromagnetic modeling, and the need for a priori

information (e.g. incident MR electric field), which is not always available. Nevertheless, some promising results have been obtained for EPT (19–22).

Instead of relying on analytical or algebraic reconstruction techniques derived from electromagnetic theory, in this work we investigate the feasibility of using data driven, supervised deep learning (DL) approach for EPs reconstructions. Deep learning approaches have recently been successfully applied to inverse problems including MRI image reconstruction (23–27). To the best of our knowledge, this is the first time that deep learning is used for EPs reconstructions. Hereafter, we refer to this approach as Deep Learning Electrical Properties Tomography (DL-EPT).

Given the promising performance of CNNs, and in particular of Conditional Generative Adversarial Network (cGAN) (28), in this work we train a cGAN to perform EPT reconstructions. Contrary to most MR-EPT techniques which make assumptions on electromagnetic quantities that are not directly accessible with MRI, in DL-EPT we can learn a surrogate analytical reconstruction model using only MR accessible quantities, such as the magnitude of the MR transmit field ( $\tilde{B}_1^+$ ) and the transceive phase ( $\varphi^\pm$ ). The training dataset is generated by electromagnetic simulations including realistic RF coil models and body models. Nowadays, these datasets can be easily generated by exploiting the availability of sophisticated electromagnetic solvers, which allow realistic electromagnetic simulations (e.g. Sim4Life; CST; COMSOL; Remcom). In this way, a high degree of a priori knowledge, such as the MRI coil setup, can be introduced to obtain robustness towards noise.

In this work, DL-EPT reconstructions from simulations on phantoms and human head models, as well as from phantom and in-vivo MR measurements using a clinically available MR setup are presented. The accuracy and precision of the reconstructed EPs maps is assessed, and the impact of different SNR levels has also been investigated. For comparison purposes, Helmholtz based MR-EPT reconstructions for the phantoms and head model simulations are presented as a reference. Although the aim of this study is a proof of principle of DL-EPT, and not an investigation into optimal network and choice of learning parameters, several options are considered. In particular, two cGANs are used:  $cGAN_{\text{mask}}$ , and  $cGAN_{\text{tissue}}$ . The former has as input the MR transit  $\tilde{B}_1^+$  field magnitude, the phase  $\tilde{\varphi}^+$  (proportional to the transceive phase  $\varphi^\pm$ ), and a binary mask (1: tissue, 0: air). In the latter, the binary mask is replaced by pseudo Spin Echo MRI images providing tissue contrast information. To the best of our knowledge, with this work we show for the first time that deep learning can provide greatly improved reconstructions of electrical conductivity and permittivity using clinically available MRI scanners, coil setups, and realistic SNR levels.

## Results

In Fig 1, standard MR-EPT and DL-EPT reconstructions are presented for the phantom model 42 with realistic noise levels. This phantom was used for in-silica testing of the selected  $cGAN_{\text{mask}}$  (see SI Appendix). Additionally, reconstructions from MRI measurements at 3T are presented for a cylindrical, homogeneous phantom with the same EPs values. The mean and standard deviation values of the reconstructed EPs maps are also reported in Fig. 1. To avoid boundary regions that cannot be reconstructed accurately in MR-EPT, a smaller region of interest was considered for this calculation (see SI Appendix).

Phantom MR-EPT reconstructions on simulated data show accurate mean EPs values after exclusion of boundary regions. However, the reported high standard deviation values indicate strong variability in the reconstructed EPs values due to noise amplification (see absolute error maps in SI Appendix). The need of high SNR levels is one of the main limitation of current analytical MR-EPT reconstruction methods.

On the contrary, DL-EPT reconstructions on simulated phantom data are less affected by noise (relative error  $< 5\%$ ) and show accurate EPs reconstructions in both homogeneous regions and at boundaries (see profiles in SI Appendix).

DL-EPT reconstructions from MR measurements confirm the results observed in simulations. These results show the feasibility of reconstructing EPs from MR measurements using DL-EPT. Additionally, permittivity reconstructions are now feasible at 3T, contrary to MR-EPT.

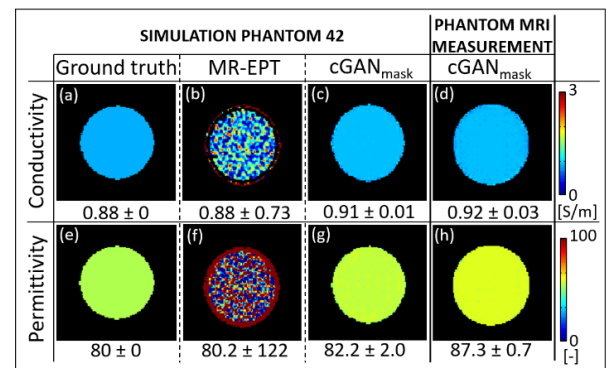


**Fig. 1:** Conductivity and permittivity maps reconstructed using MR-EPT (b, f) and  $cGAN_{\text{mask}}$  (c, d, g, h) for the phantom model 42 and phantom MRI measurements at 3 Tesla. The reported numbers are the mean  $\pm$  standard deviations values (the adopted region of interest is shown in the SI Appendix).

In Fig. 2, MR-EPT,  $cGAN_{\text{mask}}$ , and  $cGAN_{\text{tissue}}$  EPs reconstructions are shown for the head model Duke M0, which was used for in-silica testing with realistic noise levels. Mean and standard deviation values for the WM, GM, and CSF tissues are reported in Tab. 1, after eroding each tissue by 3 voxels to avoid boundary errors in MR-EPT reconstructions.

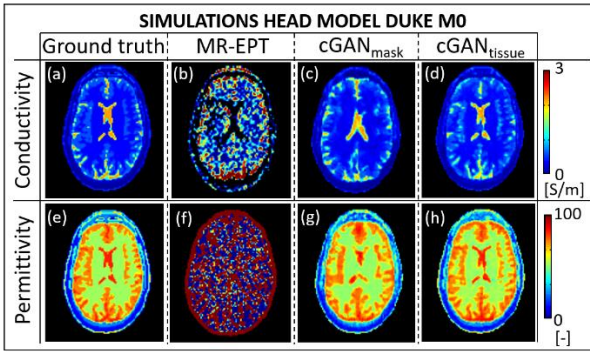


**Fig. 2:** Head Model Duke M0 conductivity and permittivity reconstructions at 3 Tesla: (a, e) Ground truth, (b, f) MR-EPT, (c, g)  $cGAN_{\text{mask}}$ , (d, h)  $cGAN_{\text{tissue}}$ .

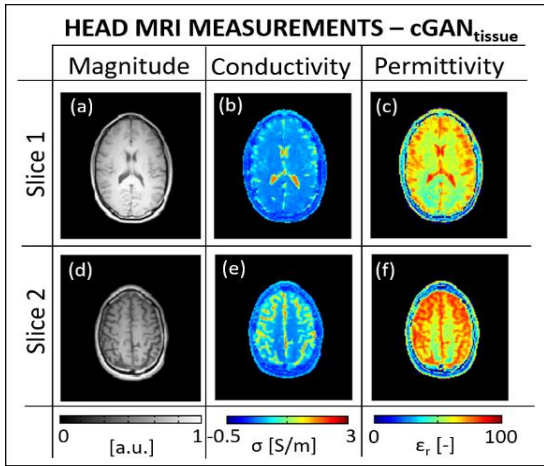


**Fig. 3:**  $cGAN_{\text{tissue}}$  EPs reconstructions from MR measurements on a healthy volunteer: (a, d) MRI magnitude images as a reference, (b, e) conductivity reconstructions, (c, f) permittivity reconstructions.

MR-EPT conductivity reconstructions are severely affected by noise and boundary errors, as previously observed for the phantom reconstructions. Although average MR-EPT conductivity and permittivity values for WM and GM have a relative error  $< 10\%$  with respect to literature values, the high standard deviations indicate that MR-EPT is not suitable to reconstruct EPs on a voxel basis for highly spatially convoluted tissue structures.

If  $cGAN_{\text{mask}}$  is used, accurate mean EPs values in the WM, GM, and CSF can be obtained (relative errors  $< 5\%$ ), except for  $\sigma_{\text{CSF}}$ . If tissue contrast information is included as input for the neural network ( $cGAN_{\text{tissue}}$ ), EPs reconstructions are more accurate for the CSF tissue. Furthermore,  $cGAN_{\text{tissue}}$  EPs reconstructions have lower standard deviation values than  $cGAN_{\text{mask}}$ ,

	Conductivity $\sigma$ [S/m]						Permittivity $\epsilon_r$ [-]					
	WM		GM		CSF		WM		GM		CSF	
	mean	[std]	mean	[std]	mean	[std]	mean	[std]	mean	[std]	mean	[std]
MR-EPT Duke M0	0.30	[0.85]	0.64	[1.27]	3.22	[5.05]	51.9	[130]	71.8	[132]	-43	[350]
$cGAN_{\text{mask}}$ Duke M0	0.34	[0.15]	0.56	[0.18]	1.83	[0.42]	52.5	[3.9]	72.9	[6.5]	84.1	[3.1]
$cGAN_{\text{tissue}}$ Duke M0	0.34	[0.03]	0.60	[0.05]	2.03	[0.14]	53.1	[1.3]	74.3	[2.1]	84.4	[1.2]
$cGAN_{\text{tissue}}$ in-vivo MRI	0.37	[0.04]	0.53	[0.18]	1.67	[0.47]	54.4	[3.2]	66.0	[6.9]	80.1	[4.9]
Reference	0.34	[-]	0.59	[-]	2.14	[-]	52.6	[-]	73.4	[-]	84	[-]

**Table 1:** Mean and Standard deviation values of the reconstructed EPs in the WM, GM, and CSF for the Head model Duke M0 using MR-EPT,  $cGAN_{\text{mask}}$ , and  $cGAN_{\text{tissue}}$ , and from in-vivo MR measurements using  $cGAN_{\text{tissue}}$ . A 3 voxels erosion was performed for each tissue type to avoid boundary regions, which cannot be reconstructed accurately with MR-EPT.

indicating less boundary errors (see absolute error maps in SI Appendix).

In Fig. 3, DL-EPT reconstructions from in-vivo MR measurements at 3T on a healthy volunteer are shown for  $cGAN_{\text{tissue}}$ . Mean and standard deviation values are also reported in Tab. 1. The reconstructed EPs values are globally accurate and tissue boundaries are preserved. This confirms what was previously observed for DL-EPT reconstructions from simulated data and shows the feasibility of using cGANs to reconstruct in-vivo EPs from MR measurements.

Finally, in Fig. 4, a comparison between MR-EPT and  $cGAN_{\text{mask}}$  EPs reconstructions for the head model Duke M0 with a tumor inclusion is presented. Mean EPs values of the tumor inclusion and standard deviations values are also reported. Correct identification of the tumor region is difficult for MR-EPT reconstructions, which are highly corrupted by noise. Instead,  $cGAN_{\text{mask}}$  EPs reconstructions clearly show a tissue-tumor contrast, especially in the permittivity map. The presented DL-EPT reconstructions show an underestimation for the tumor conductivity value (relative error  $\approx 15\%$ ), while the reconstructed tumor permittivity value is accurate (relative error  $< 5\%$ ).

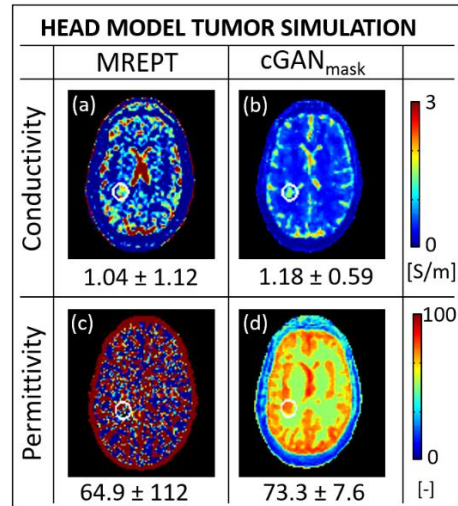


**Fig. 4:** MR-EPT and  $cGAN_{\text{mask}}$  EPs reconstructions for Duke M0 – Tumor model. The tumor contour is highlighted with a white circle. The EPs of the tumor are respectively:  $\sigma = 1.4$  S/m;  $\epsilon_r = 73$ . The numbers reported in the Fig. are the mean  $\pm$  the standard deviations of the EPs values of the tumor inclusion.



## Discussion

In this work, a novel approach for EPs reconstructions is presented, namely deep learning electrical properties tomography (DL-EPT). This technique is based on a data driven learning task where the training data are obtained by performing a large number of realistic electromagnetic simulations. We show for the first time that DL-EPT allows accurate and precise conductivity and permittivity reconstructions of human brain tissues at clinically available MR field strengths. This has been investigated using in-silica realistic phantom and head data, as well as phantom and in-vivo MR measurements at 3 Tesla. The presented results show good accuracy and most notably precision in the reconstructed EPs maps on a voxel basis, demonstrating a large improvement with respect to conventional Helmholtz MR-EPT. Furthermore, DL-EPT is noise-robust and preserves boundary information, while these two aspects are the major issues for conventional MR-EPT.

The DL-EPT method differs significantly from conventional MR-EPT techniques employing analytical or algebraic reconstruction models. The popular Helmholtz MR-EPT technique, an example of an analytical reconstruction technique, requires the computation of spatial derivatives on measured data (13). This computation is performed by convolving the measured, complex  $\tilde{B}_1^+$  field with large finite difference kernels such as the 3D kernel adopted in this work (10), or the Savitzky-Golay kernel (29). These kernels, combined with image filters to suppress the impact of noise (17, 21), lead to a much coarser effective resolution (order of 1 cm) and result in severe errors at tissue boundaries.

On the other hand, algebraic MR-EPT reconstruction techniques employing iterative minimization, such as CSI-EPT (19), should be more noise-robust. However, these methods require a large degree of regularization to stabilize noise augmentation in specific regions and, therefore, high quality experimental reconstructions are not yet available. Furthermore, these reconstruction techniques employ forward models formulated in electromagnetic quantities that are not always accessible with MRI, such as the phase of the transmit MR field and the incident electric field.

Given these limitations for conventional MR-EPT reconstructions, we investigated the feasibility of using supervised deep learning to reconstruct EPs from accessible MR quantities. Crucial for the success of DL-EPT is the training part where a large degree of a priori knowledge can be introduced by simulating a realistic coil setup and including realistic head models. The training requires a high number of unique complex  $\tilde{B}_1^+$  fields. Unique  $\tilde{B}_1^+$  distributions including the transceive phase can be obtained by means of sophisticated, realistic electromagnetic simulations, which are nowadays possible with commonly available electromagnetic simulation software. Therefore, realistic electromagnetic simulations are an elegant solution to overcome the need of a high amount of MR data for training.

Our results indicate that not only conductivity reconstructions at clinical MRI field strengths are

feasible, but also permittivity maps can be obtained using DL-EPT. The latter were not yet feasible with conventional MR-EPT approaches due to insufficient SNR levels at clinical field strengths (1.5 and 3 Tesla) (12, 30). Preliminary investigations indicate that the adopted cGAN is highly noise-robust. Erroneous EPs reconstructions appear at SNR levels around 20 (see SI Appendix). Ultimately, the noise-robustness of DL-EPT is highly appealing, as it would permit to relax the requirements in terms of MRI data acquisition, allowing EPs measurements in clinical settings.

Of course, the use of a priori knowledge during training could also create biased reconstruction for cases not included in the training phase. This would generally be the case for patients with pathologies. To test this risk, we provided the cGAN<sub>mask</sub> with a pathological case that was not present in the training set, i.e. a head model including a brain tumor with altered EPs. In case of overfitting, which is a known issue for deep learning, reconstructions would not work anymore. Preliminary results at 3 Tesla show that DL-EPT can provide a better tumor-normal tissue contrast than MR-EPT. Possibly, the inclusion of realistic tumor models in the training set could be beneficial for accurate DL-EPT reconstructions for brain cancer applications. This requires further investigations.

Furthermore, it will be interesting to investigate whether EPs can also be reconstructed for different body parts than the one used during training. This would increase the applicability of DL-EPT without the need of dedicated training sets. Still, if specific databases are needed, they can be easily constructed by means of realistic electromagnetic simulations. Future works should address this question.

In conclusion, to the best of our knowledge, this is the first demonstration of the feasibility of reconstructing in-vivo EPs from MR measurements using supervised deep learning. Although this work is a first proof of principle without aiming at identifying the best network architecture, which is beyond the current scope, the presented results indicate major improvements in the quality of the reconstructed EPs maps compared to MR-EPT approaches. Even permittivity reconstructions are now feasible at 3T with a widely available coil setup.

We showed that DL-EPT is noise-robust, thus the requirements in terms of SNR can be relaxed. This will allow faster imaging protocols and higher spatial resolutions. Furthermore, we demonstrated that DL-EPT is feasible at clinically available field strengths with standard coil setups. Moreover, DL-EPT can be trained to work with the accessible transceive phase, thus circumventing the issue that the  $\tilde{B}_1^+$  phase is not directly accessible with MRI. Finally, we believe that the major impact of this work is that the application of supervised learning for EPT reconstructions greatly improves the quality of the EP maps. We believe that this could be a key innovation step to turn EPT into a reliable, sensitive clinical biomarker revealing important information on tissue ionic composition as a surrogate of a different metabolism caused by pathological conditions.

## Materials and Methods

**Database Construction.** A database consisting of 42 homogeneous phantom models (diameter: 12 cm, length: 12 cm) and 20 head models with piecewise constant EPs values was created in Sim4Life (ZMT AG, Zurich, CH). Different EPs values were assigned to each phantom model and to the WM, GM, and CSF tissue of the adopted head models (Duke and Ella, the Virtual Family (31)) (see SI Appendix). These models were placed inside a realistic birdcage body coil model resonant at 128 MHz, thus mimicking the experimental MR setup. With this setup, FDTD simulations were performed in Sim4Life to obtain realistic  $B_1^+$  field magnitude and transceive phase ( $\varphi^\pm$ ) maps. Thermal noise was included by independently adding Gaussian noise to the real and imaginary parts of the computed complex  $\tilde{B}_1^+$  field, which includes the simulated  $B_1^+$  field magnitude and transceive phase  $\varphi^\pm$ . The final SNR was 90 for the obtained  $\tilde{B}_1^+$  magnitude and the precision of the obtained phase  $\tilde{\varphi}^+$ , proportional to the transceive phase  $\varphi^\pm$ , was  $9 \times 10^{-3}$  rad (see SI Appendix). This mimics realistic SNR levels in MR experiments. By means of these simulations, 2170 unique complex  $\tilde{B}_1^+$  field distributions were generated (25 slices for each phantom model and 56 slices for each head model).

**Neural Network.** The neural network used for EPs reconstructions was a Conditional Generative Adversarial Network (cGAN). In this type of networks, two sub-networks (generator G, and discriminator D) compete with each other in a min-max optimization game during the training phase, in order to learn a conditional generative model. The generator network tries to generate EPs maps from the input images, while the discriminator network tries to discriminate the generated EPs maps from the EPs maps in the training set (ground truth). Like in (28), the generator was a U-Net and the discriminator was a convolutional PatchGAN classifier. In (32), it was shown that using a cGAN combined with a L2 norm is beneficial to alleviate the blurry effect caused by the L2 norm. Afterwards, in (28) it was demonstrated that the use of the L1 norm further reduces blurring in the reconstructed images. For EPs reconstructions, it is important to achieve good accuracy at tissues boundaries. Based on these observations, the following cost function ( $F$ ) was adopted in this work:

$$F = \arg \min_G \max_D \lambda_{cGAN} \mathcal{L}_{cGAN}(G, D) + \lambda_{L1} \mathcal{L}_{L1}(G) + \lambda_{L2} \mathcal{L}_{L2}(G) \quad [1]$$

where  $\mathcal{L}_{cGAN}(G, D)$  is the GAN objective,  $\mathcal{L}_{L1}$  and  $\mathcal{L}_{L2}$  are respectively the L1 and L2 distance between the ground truth and the output, and  $\lambda_{cGAN}$ ,  $\lambda_{L1}$ , and  $\lambda_{L2}$  are the corresponding weights (see SI Appendix for the details).

This network was implemented in TensorFlow (33) and trained in about four hours on a GPU NVIDIA Tesla P100 16GB RAM. After training, EPs reconstructions could be performed in less than 1 minute for a 3D volume of  $256 \times 256$  voxels in plane and 56 slices.

**Training, Validation, and Testing.** For the training, 2014  $\tilde{B}_1^+$  field distributions were generated using all the models except for the phantom models 12, 24, 38, and 42, and the head model Duke M0. The inputs for the network were: the  $\tilde{B}_1^+$  magnitude, the phase  $\tilde{\varphi}^+$  (proportional to the transceive phase  $\varphi^\pm$ ), and a binary mask (1: object, 0: air). We define this network as  $cGAN_{mask}$ , since the third input was a binary mask. To reduce the complexity of the problem, two networks were trained separately for conductivity and permittivity using the same combination of  $\lambda$ -weights. For the validation, the  $\tilde{B}_1^+$  field distributions of the phantom models 12 and 24 were used. Although the aim of the paper was not to find the best combination of  $\lambda_{GAN}$ ,  $\lambda_{L1}$ , and  $\lambda_{L2}$  weights, we investigated the impact of various combinations of these parameters on the reconstructed EPs maps. The parameter combination with the lowest average normalized-root-mean-square error (NRMSE) computed over all conductivity and permittivity reconstructions from the validation set was selected for testing. The selected combination was:  $\lambda_{GAN} = 2$ ,  $\lambda_{L1} = 100$ , and  $\lambda_{L2} = 200$  (see SI Appendix). Furthermore, a U-Net could be obtained by setting  $\lambda_{GAN} = 0$  (34). We therefore investigated whether using the less sophisticated U-Net would be sufficient for EPs reconstructions using the model Duke M0 (see SI Appendix).

For testing of the selected  $cGAN_{mask}$ , the  $\tilde{B}_1^+$  field distributions of the phantom models 38 and 42, and Duke model M0 were used. The performed realistic electromagnetic simulations provide a controlled environment in which knowledge of the ground truth, i.e. conductivity and permittivity, is possible. This ensured correct assessment of the accuracy (absolute errors:  $\Delta\sigma$ , and  $\Delta\epsilon_r$ ) and precision (standard deviation) of the performed EPs reconstructions. Additionally, this network was tested on measured MRI data using a homogeneous, agar-based phantom: diameter: 13 cm, length: 15 cm,  $\sigma$ : 0.88 S/m;  $\epsilon_r$ : 80, obtained from probe measurements at 21°C (85070E, Agilent Technologies, Santa Clara, CA, USA).

Since MRI provides specific tissue contrast, we investigated whether using this information as third input instead of using a simple mask would improve the EPs reconstructions for the human brain and the selected cGAN. We therefore trained a cGAN with the previously chosen combination of  $\lambda$ -weights and only the  $\tilde{B}_1^+$  field distributions of the brain models, except for Duke M0, which was used for testing. Hence, the inputs were: the  $\tilde{B}_1^+$  magnitude, the phase  $\tilde{\varphi}^+$ , and pseudo Spin echo magnitude images obtained after assigning to each tissue type the corresponding magnitude value that would be measured in those tissues using a Spin Echo sequence (see SI Appendix). We define this network as  $cGAN_{tissue}$ , since the third input provides tissue information. This network was tested using Duke M0 and in-vivo MRI data of a healthy volunteer (male, 29 years old), after obtaining written informed consent.

Finally, we investigated the feasibility of detecting a tumor without providing any information on tissue structure and without having trained the  $cGAN_{mask}$

with tumor regions. For this purpose, a head tumor model was created by placing one sphere inside Duke M0 (radius 1.5 cm,  $\sigma$ : 1.4 S/m;  $\epsilon_r$ : 73). The parameter combination with the lowest average NRMSE value computed over conductivity and permittivity reconstructions in the WM, GM and CSF of Duke M0 was chosen for this test:  $\lambda_{GAN} = 2$ ,  $\lambda_{L1} = 1000$ , and  $\lambda_{L2} = 2000$  (see SI Appendix).

**MRI Measurements.** MRI measurements were performed with a 3 Tesla MR scanner (Ingenia, Philips HealthCare, Best, The Netherlands) with the body coil in transmit and a 15-channel head coil in receive mode. The  $\tilde{B}_1^+$  magnitude was measured using a dual-TR (AFI) sequence (35). To map the transceive phase ( $\varphi^\pm$ ) two single echo Spin Echo (SE) sequences with opposite readout gradient polarities were combined (10):  $\varphi^\pm = (\varphi_{SE1} - \varphi_{SE2})/2$ , thus minimizing the impact of eddy-currents. To convert the receive phase measured with the head coil to the body coil, as if the body coil would have been used both for transmitting and receiving, the vendor specific algorithm CLEAR (Constant Level of Appearance) was used. The sequence parameters for the phantom and the in-vivo MRI measurements are reported in the SI Appendix.

**MR-EPT Reconstructions.** For comparison purposes, standard Helmholtz MR-EPT reconstructions were also performed on the same models adopted for the testing of the selected cGAN<sub>mask</sub>, i.e. phantom models 38 (see SI Appendix), and 42, and on the head model Duke M0, according to (10):

$$\epsilon_r(\mathbf{r}) = \frac{-1}{\mu_0 \epsilon_0 \omega^2} \text{Re} \left( \frac{\nabla^2 \tilde{B}_1^+(\mathbf{r})}{\tilde{B}_1^+(\mathbf{r})} \right) \quad [2]$$

$$\sigma(\mathbf{r}) = \frac{1}{\mu_0 \omega} \text{Im} \left( \frac{\nabla^2 \tilde{B}_1^+(\mathbf{r})}{\tilde{B}_1^+(\mathbf{r})} \right) \quad [3]$$

with  $\omega$ : Larmor angular frequency,  $\epsilon_0/\mu_0$ : free space permittivity/permeability, and  $\mathbf{r}$ : x/y/z-coordinates. To compute the second order spatial derivatives, a 3D noise-robust kernel was used ( $7 \times 7 \times 5$  voxels) (10).

## References

1. Katscher U, Kim DH, Seo JK (2013) Recent progress and future challenges in MR electric properties tomography. *Comput Math Methods Med* (ID 546562):1–11.
2. Katscher U, van den Berg C a. T (2017) Electric properties tomography: Biochemical, physical and technical background, evaluation and clinical applications. *NMR Biomed*:early view.
3. van Lier ALHMW, et al. (2011) Electrical conductivity imaging of brain tumours. *Proc 19th Annu Meet ISMRM Montréal, Québec, Canada*:4464.
4. Katscher U, et al. (2012) Estimation of breast tumor conductivity using parabolic phase fitting. *Proc 20th Sci Meet Int Soc Magn Reson Med Melbourne, Victoria, Aust*:2335.
5. Shin J, et al. (2014) Initial study on in vivo conductivity mapping of breast cancer using MRI. *J Magn Reson Imaging*:371–378.
6. Balidemaj E, et al. (2016) In vivo electric conductivity of cervical cancer patients based on B1+ maps at 3T MRI. *Phys Med Biol* 61(4):1596–1607.
7. Kim SY, et al. (2016) Correlation between conductivity and prognostic factors in invasive breast cancer using magnetic resonance electric properties tomography (MREPT). *Eur Radiol* 26(7):2317–2326.
8. Haacke EM, Petropoulos LS, Nilges EW, Wu DH (1991) Extraction of conductivity and permittivity using magnetic resonance imaging. *Phys Med Biol* 38:723–734.
9. Katscher U, et al. (2009) Determination of Electric Conductivity and Local SAR Via B1 Mapping. *IEEE Trans Med Imaging* 28(9):1365–1374.
10. van Lier ALHMW, et al. (2012) B1+ phase mapping at 7 T and its application for in vivo electrical conductivity mapping. *Magn Reson Med* 67:552–561.
11. van Lier ALHMW, et al. (2014) Electric properties tomography in the human brain at 1.5, 3, and 7 T: a comparison study. *Magn Reson Med* 71:354–363.
12. Lee S, Bulumulla S, Hancu I (2015) Theoretical Investigation of Random Noise-Limited Signal-to-Noise Ratio in MR-Based Electrical Properties Tomography. *IEEE Trans Med Imaging* 34(11):2220–2232.
13. Mandija S, Sbrizzi A, Katscher U, Luijten PR, van den Berg C a. T (2017) Error analysis of helmholtz-based MR-electrical properties tomography. *Magn Reson Med*:early view.
14. Sodickson DK, et al. (2013) Generalized Local Maxwell Tomography for Mapping of Electrical Property Gradients and Tensors. *Proc 21st Sci Meet Int Soc Magn Reson Med Salt Lake City, Utah, USA*:4175.
15. Hafalir FS, Oran OF, Gurler N, Ider YZ (2014) Convection-reaction equation based magnetic resonance electrical properties tomography (cr-MREPT). *IEEE Trans Med Imaging* 33(3):777–793.
16. Liu J, Zhang X, Schmitter S, Van de Moortele P-F, He B (2015) Gradient-based electrical properties tomography (gEPT): A robust method for mapping electrical properties of biological tissues in vivo using magnetic resonance imaging. *Magn Reson Med* 74:634–646.
17. Gurler N, Ider YZ (2016) Gradient-Based Electrical Conductivity Imaging Using MR Phase. *Magn Reson Med* 77:137–150.

18. Marques JP, Sodickson DK, Ipek O, Collins CM, Gruetter R (2015) Single acquisition electrical property mapping based on relative coil sensitivities: A proof-of-concept demonstration. *Magn Reson Med* 74(1):185–195.
19. Balidemaj E, et al. (2015) CSI-EPT: A Contrast Source Inversion Approach for Improved MRI-Based Electric Properties Tomography. *IEEE Trans Med Imaging* 34(9):1788–1796.
20. Borsic A, Perreard I, Mahara A, Halter RJ (2016) An inverse problems approach to MR-EPT image reconstruction. *IEEE Trans Med Imaging* 35(1):244–256.
21. Ropella KM, Noll DC (2017) A regularized, model-based approach to phase-based conductivity mapping using MRI. *Magn Reson Med* 78:2011–2021.
22. Serralles JE, et al. (2016) Global Maxwell Tomography: A novel technique for electrical properties mapping without symmetry assumption or edge artifacts. *Proc 24th Sci Meet Int Soc Magn Reson Med Singapore*:2993.
23. Vladimir G, et al. (2015) q-Space Deel Learning for Twelve-Fold Shorter and Model Free Diffusion MRI Scans. *MICCAI*:37–44.
24. Hammernik K, et al. (2018) Learning a variational network for reconstruction of accelerated MRI data. *Magn Reson Med* 79:3055–3071.
25. Işin A, Direkoğlu C, Şah M (2016) Review of MRI-based Brain Tumor Image Segmentation Using Deep Learning Methods. *Procedia Comput Sci* 102:317–324.
26. Hyun CM, Kim HP, Lee SM, Lee S, Seo JK (2017) Deep learning for undersampled MRI reconstruction. *arXiv* 1709.02576:1–11.
27. Zhu B, Liu JZ, Rosen BR, Rosen MS (2018) Image reconstruction by domain transform manifold learning. *Nature* 555:487–492.
28. Isola P, Zhu J-Y, Zhou T, Efros AA (2016) Image-to-Image Translation with Conditional Adversarial Networks. *arXiv* 1611.07004:1–16.
29. Savitzky A, Golay MJE (1964) Smoothing and Differentiation of Data by Simplified Least Squares Procedures. *Anal Chem* 36:1627–1639.
30. Duan S, et al. (2016) Quantitative analysis of the reconstruction errors of the currently popular algorithm of magnetic resonance electrical property tomography at the interfaces of adjacent tissues. *NMR Biomed* 29:744–750.
31. Christ A, et al. (2010) The Virtual Family - Development of surface-based anatomical models of two adults and two children for dosimetric simulations. *Phys Med Biol* 55(2):23–38.
32. Pathak D, Krahenbuhl P, Donahue J, Darrell T, Efros A a. (2016) Context Encoders: Feature Learning by Inpainting. *arXiv* 1604.07379:12.
33. Abadi M, et al. (2016) TensorFlow: Large-Scale Machine Learning on Heterogeneous Distributed Systems. *arXiv* 1603.04467:1–19.
34. Ronneberger O, Fischer P, Brox T (2015) U-Net: Convolutional Networks for Biomedical Image Segmentation. *arXiv* 1505.04597:234–241.
35. Yarnykh VL (2007) Actual flip-angle imaging in the pulsed steady state: A method for rapid three-dimensional mapping of the transmitted radiofrequency field. *Magn Reson Med* 57(1):192–200.



# Opening a new window on MR-based Electrical Properties Tomography with deep learning – *Supporting Information*

Stefano Mandija<sup>1</sup>, Ettore F. Meliadd<sup>1,2</sup>, Niek Huttinga<sup>1</sup>,  
Peter R. Luijten<sup>1,3</sup>, Cornelis A.T. van den Berg<sup>1,4</sup>

<sup>1</sup> Center for Image Sciences, University Medical Center Utrecht, Heidelberglaan 100, Utrecht, 3584 CX, The Netherlands.

<sup>2</sup> MR Code BV, Schimminck 18, Zaltbommel, 5301 KR, The Netherlands.

<sup>3</sup> Department of Radiology, University Medical Center Utrecht, Heidelberglaan 100, Utrecht, 3584 CX, The Netherlands.

<sup>4</sup> Department of Radiotherapy, University Medical Center Utrecht, Heidelberglaan 100, Utrecht, 3584 CX, The Netherlands.

**In submission to PNAS (<http://www.pnas.org/>)**

---

## Table of Contents

<b>List of Figures – Tables</b>	2
<b>Supporting Information Methods</b>	
Part A: Phantom and Head Models	3
Part B: Sim4Life Simulations and Database Construction	6
Part C: Choice of cGAN <sub>mask</sub>	8
Part D: MR Sequences – Parameters	9
<b>Supporting information Results</b>	
Part A: Phantom EPs Reconstructions – Profiles and Absolute Errors	10
Part B: Head Model EPs Reconstructions – Absolute Errors	12
<b>Supporting Information Discussion</b>	
Part A: Impact of SNR	13
Part B: Comparison U-Net and cGANs	14

## List of Figures

Fig. 1A-SImethods	Head models: conductivity maps	4
Fig. 2A-SImethods	Head models: permittivity maps	5
Fig. 1B-SImethods	Electromagnetic simulations setup	6
Fig. 2B-SImethods	Flowchart, from simulations to cGANs inputs	6
Fig. 3B-SImethods	cGANs inputs/outputs	7
Fig. 4B-SImethods	MRI Spin Echo and pseudo Spin Echo maps	8
Fig. 1A-SIresults	Phantom Model 42, EPs profiles	10
Fig. 2A-SIresults	Phantom Model 42, EPs absolute error maps	11
Fig. 3A-SIresults	Phantom Model 38 MR-EPT and DL-EPT reconstructions	11
Fig. 1B-SIresults	Head Model Duke M0, EPs absolute error maps	12
Fig. 1A-SIdiscussion	Impact of SNR on EPs reconstruction for the Head Model Duke M0	13
Fig. 1B-SIdiscussion	U-Net VS cGANs EPs reconstruction for the Head Model Duke M0	14

## List of Tables

Tab. 1A-SImethods	Phantom Models: ground truth EPs values	3
Tab. 2A-SImethods	Head Models: ground truth EPs values and geometrical transformations	3
Tab. 1B-SImethods	MRI Spin Echo and pseudo Spin Echo signal intensity	8
Tab. 1C-SImethods	Phantom Models 12 and 24: mean EPs and standard deviation values	9
Tab. 1D-SImethods	MRI sequence parameters: AFI sequence	9
Tab. 2D-SImethods	MRI sequence parameters: Spin Echo sequences	9
Tab. 1A-SIdiscussion	Head Model Duke M0 EPs reconstructions: impact of SNR	13
Tab. 2A-SIdiscussion	Head Model Duke M0 EPs reconstructions: U-Net VS cGANs	14

## SUPPORTING INFORMATION METHODS

### Part A: Phantom and Head Models

In this first section, the ground truth EPs values of the adopted 42 phantom models (Tab. 1A-SImethods) and the 20 head models (Tab. 2A-SImethods) are reported. In order to introduce more variability between the adopted head models, not only the conductivity and permittivity values of WM, GM and CSF were changed between models, but also geometrical transformations were applied with respect to the original models (Duke M0 and Ella M0). These transformations include compression/dilatation of the head models, as well as rotation and translation, thus mimicking different possible head orientations inside the MR bore. For each head model, ground truth EPs maps on one slice (red plane) are shown (Fig. 1A-SImethods, and 2A-SImethods). This slice was taken on the same plane for all the 20 head models with respect to the considered volume of interest (yellow box). Therefore, the observed variability between subfigures is due to the performed geometrical transformations and variations in the EPs for the adopted 20 head models.

PHANTOM	1	2	3	4	5	6	7	8	9	10	11	12	13	14
$\sigma$ [S/m]	1.2	1.25	1.3	1.35	1.4	1.45	1.5	1.55	1.6	1.65	1.7	1.75	1.8	1.85
$\epsilon_r$ [-]	81	70	60	65	75	85	72	82	62	83	73	63	88	68
PHANTOM	15	16	17	18	19	20	21	22	23	24	25	26	27	28
$\sigma$ [S/m]	1.9	1.95	2	2.05	2.1	2.15	2.2	0.2	0.25	0.3	0.35	0.4	0.45	0.5
$\epsilon_r$ [-]	78	86	66	76	87	67	77	80	70	60	65	75	85	72
PHANTOM	29	30	31	32	33	34	35	36	37	38	39	40	41	42
$\sigma$ [S/m]	0.55	0.6	0.65	0.7	0.75	0.8	0.85	0.9	0.95	1	1.05	1.1	1.15	0.88
$\epsilon_r$ [-]	82	62	83	73	63	88	68	78	86	66	76	87	67	80

**Tab. 1A-SImethods:** The electrical properties values of the 42 phantom models. The models used for validation are highlighted in red, while the models used for testing are highlighted in green.

		Tx	Ty	Tz	WM		GM		CSF	
		[%]	[%]	[%]	$\sigma$ [S/m]	$\epsilon_r$ [-]	$\sigma$ [S/m]	$\epsilon_r$ [-]	$\sigma$ [S/m]	$\epsilon_r$ [-]
Duke	M0	1	1	1	0.34	52.6	0.59	73.4	2.14	84
	M1	1.01	1	1.005	0.35	50.5	0.56	75.5	2.10	83.0
	M2	1.015	1.01	1	0.35	51.0	0.57	72.5	2.18	84.5
	M3	1	1.01	1.02	0.33	52.0	0.58	73.0	2.08	85.0
	M4	1.01	1.02	1.02	0.36	51.0	0.56	73.2	2.15	83.5
	M5	0.95	1	1.06	0.35	53.0	0.59	74.0	2.05	84.6
	M6	1.02	0.94	0.92	0.33	51.5	0.60	73.0	2.20	81.0
	M7	0.94	1.02	1	0.34	53.0	0.60	72.0	2.16	86.0
	M8	1.02	1.02	0.94	0.35	52.0	0.59	75.0	2.06	82.5
M9	1.03	0.96	1.03	0.35	53.4	0.60	74.7	2.21	84.0	
Ella	M0	1	1	1	0.34	52.5	0.59	73.5	2.14	84.0
	M1	1.04	1.02	1	0.36	51.8	0.57	71.4	2.02	86.0
	M2	0.94	0.96	1	0.32	52.0	0.60	74.0	2.00	86.5
	M3	0.9	0.98	1.02	0.35	54.0	0.56	71.3	1.98	83.0
	M4	0.97	0.9	1	0.32	51.2	0.60	75.1	2.03	82.6
	M5	1.05	0.97	0.94	0.33	53.2	0.60	74.4	2.04	84.0
	M6	1	1.04	1.04	0.35	53.4	0.57	72.8	2.17	85.3
	M7	1	1.06	0.98	0.35	50.6	0.57	75.2	2.01	86.2
	M8	0.96	1.04	0.92	0.33	51.6	0.61	72.3	1.96	82.6
M9	1.02	1.06	0.96	0.36	54.3	0.59	72.5	2.23	80.3	

**Tab. 2A-SImethods:** The electrical properties values of the 20 head models. Tx, Ty, and Tz are the scaling factors applied to the original models along the coordinate axis x, y, and z (Tx,y,z = 1: no scaling, Tx,y,z > 1: dilatation, and Tx,y,z < 1: compression).

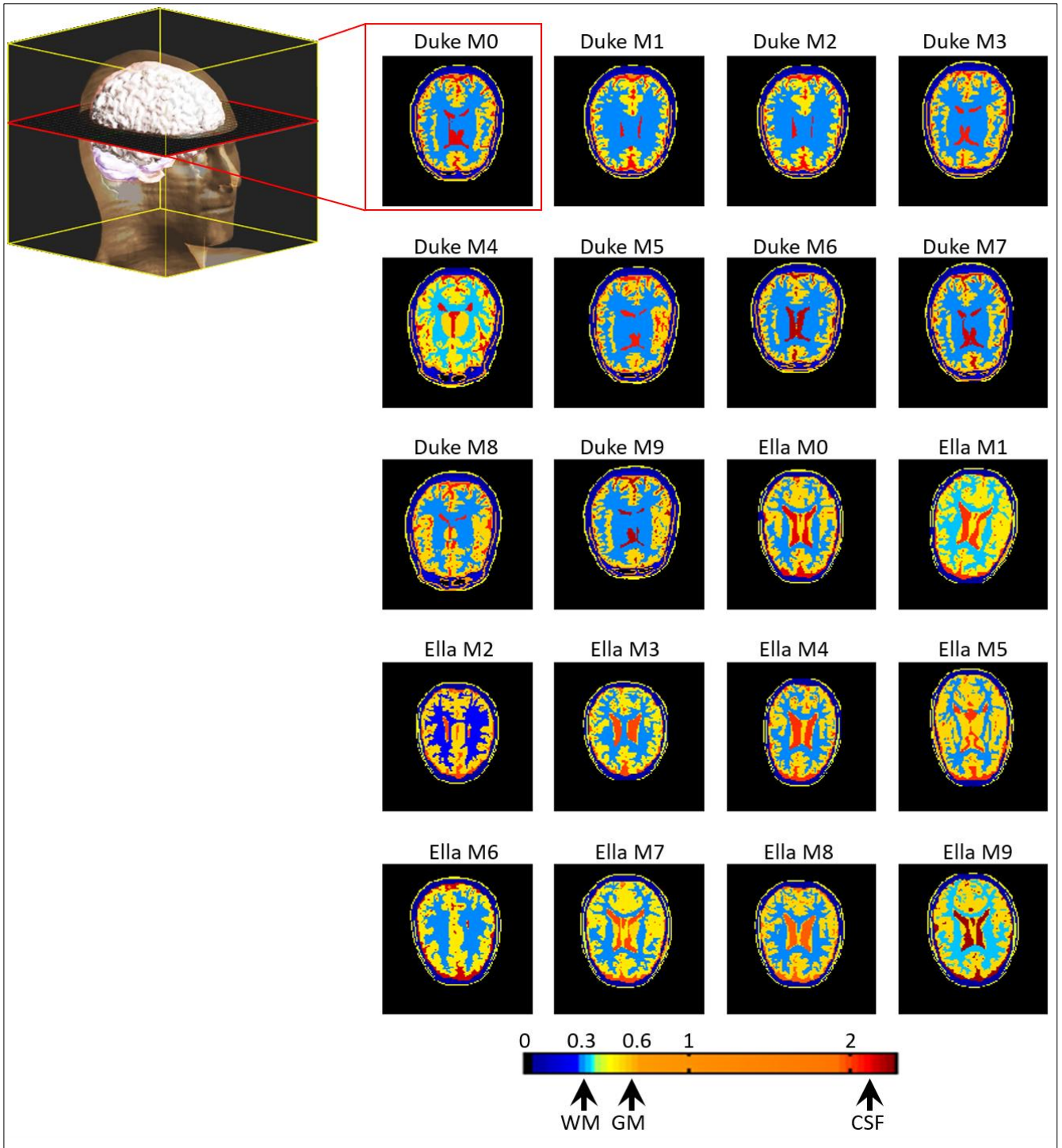


**Fig. 1A-SImethods:** Conductivity maps of the adopted 20 head models. These maps were taken on the same slice (red plane) inside the adopted volume of interest (yellow box).

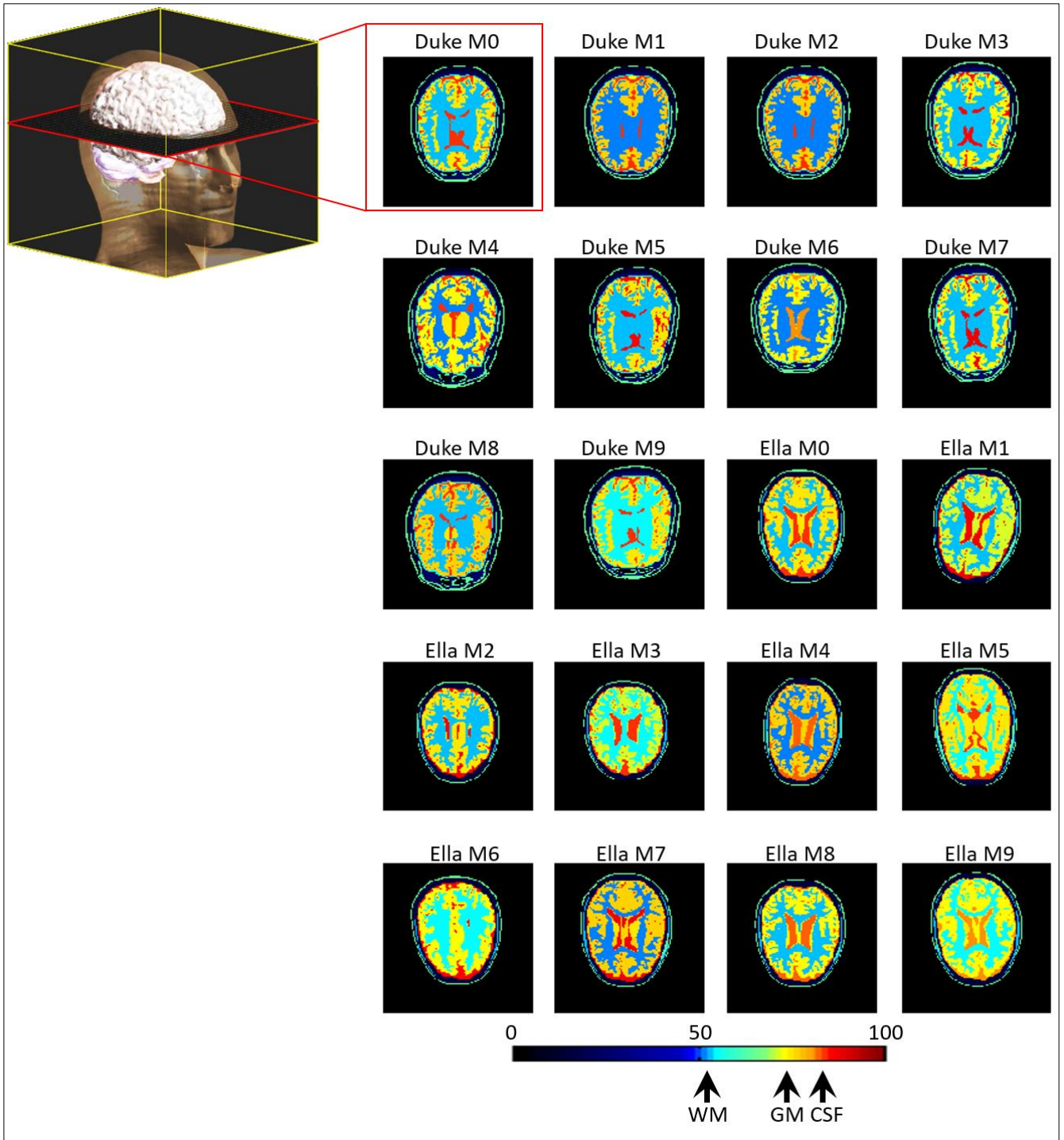


**Fig. 2A-SImethods:** Permittivity maps of the adopted 20 head models. These maps were taken on the same slice (red plane) inside the adopted volume of interest (yellow box).



## Part B: Sim4Life Simulations and Database Construction

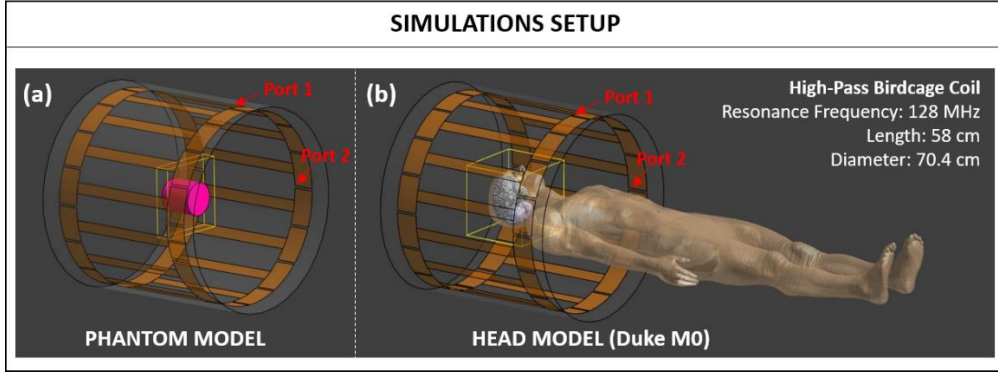


**Fig. 1B-SImethods:** The setup adopted in Sim4Life for the electromagnetic simulations on: (a) phantoms, (b) head models.

Two simulations were performed in Sim4Life for each phantom and head model (Fig. 1B-SImethods): one in quadrature mode (QA), and one in anti-quadrature mode (AQ). Contrary to conventional MR-EPT approaches which assume  $\varphi^+ \approx (\varphi^+ + \varphi^-)/2$ , here the transceive phase  $\varphi^\pm$  was adopted, i.e. the measurable phase during an MR experiment. In particular, the phase  $\hat{\varphi}^+$  was used, where  $\hat{\varphi}^+ = (\varphi^\pm/2)$ , with  $\hat{\varphi}^+ \neq \varphi^+$ , since  $\varphi^+ \neq \varphi^-$ . From these simulations, the electromagnetic quantity  $\hat{B}_1^+$  was obtained (Fig. 2B-SImethods).  $\hat{B}_1^+$  consists of the transmit  $B_1^+$  field magnitude and the phase  $\hat{\varphi}^+$ , proportional to the transceive phase  $\varphi^\pm$ . Then, Gaussian noise was independently added to the real and imaginary parts of the computed complex  $\hat{B}_1^+$  field. Finally, the magnitude and the phase of the obtained noise-corrupted  $\tilde{B}_1^+$  fields were used as inputs for the cGANs (Fig. 2B-SImethods). The SNR of  $|\tilde{B}_1^+|$  maps and the precision of  $\tilde{\varphi}^+$  maps obtained from the simulations were defined as:

$$\text{SNR}_{|\tilde{B}_1^+|} = \frac{\text{mean}(|\tilde{B}_1^+|)}{\text{std}(|\tilde{B}_1^+| - |B_1^+|)}, \quad \Delta\tilde{\varphi}^+ = \frac{1}{\text{SNR}_{|\tilde{B}_1^+|}}.$$

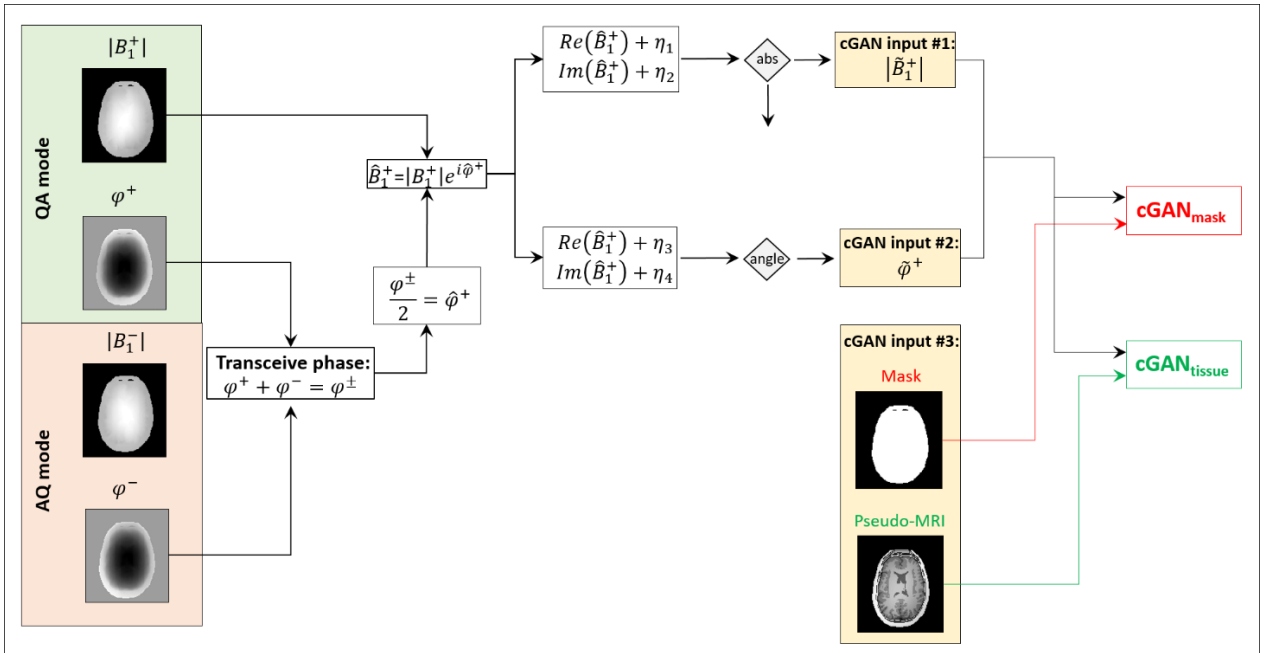


**Fig. 2B-SImethods:** Flowchart of the operations performed to create the input maps for the cGANs.

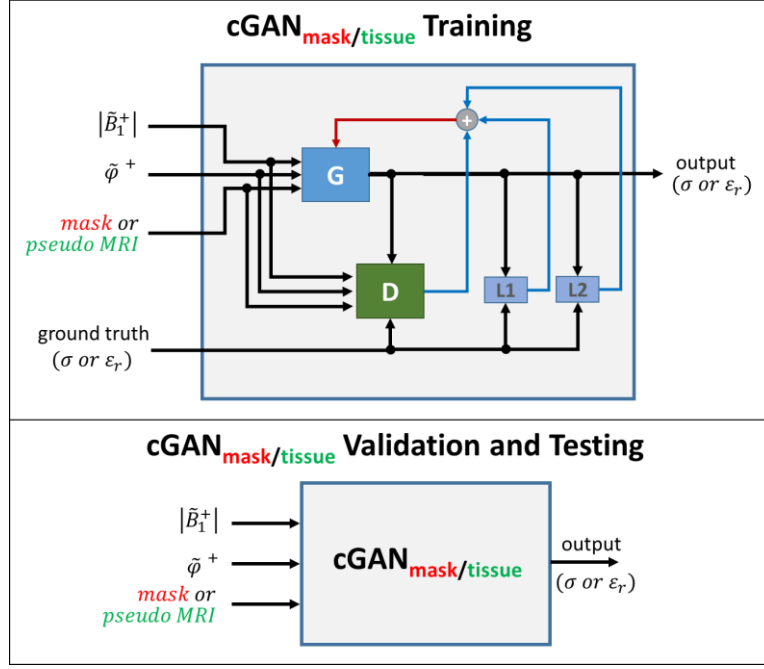


**Fig. 3B-SImethods:** Flowchart of the inputs/outputs of the adopted cGANs (cGAN<sub>mask</sub>, and cGAN<sub>tissue</sub>) for training, validation, and testing.

To reduce the complexity of the reconstruction problem, cGANs were independently trained for permittivity and conductivity reconstructions, but the same values were used for the network weights  $\lambda_{\text{GAN}}$ ,  $\lambda_{\text{L1}}$ , and  $\lambda_{\text{L2}}$ . The inputs were the magnitude of the noise-corrupted  $\tilde{B}_1^+$  field, the phase  $\tilde{\varphi}^+$ , and a binary mask (1 for tissue and 0 for air). We define this network as cGAN<sub>mask</sub>. To investigate the impact of tissue information on the accuracy of the reconstructed EPs values, pseudo Spin Echo images were used instead of the binary mask as input. We define this network as cGAN<sub>tissue</sub> (Fig. 3B-SImethods).

These pseudo Spin Echo images were created for each brain model as it follows. First, reference magnitude values were computed for each brain tissue from MRI measurements on a healthy volunteer performed using a Spin Echo sequence (see part D-SImethods below). In particular, these reference values are mean magnitude values computed for each tissue type inside regions with an homogeneous  $\tilde{B}_1^+$  magnitude field distribution. These values were applied to the corresponding tissue type of each brain model. Then, the obtained maps were scaled using the simulated  $\tilde{B}_1^+$  magnitude field distribution for each head model. Finally, Gaussian noise was added using the same SNR level adopted for the phase maps  $\tilde{\varphi}^+$ , proportional to the transceive phase  $\varphi^\pm$ .

For comparison purposes, one slice of the acquired MRI Spin Echo images on a healthy volunteer and one slice of the computed pseudo Spin Echo maps for Duke Model M0 are shown in Fig. 4B-SImethods. Mean values computed in different ROIs show good agreement between the MRI Spin Echo image and the pseudo Spin Echo image (Tab. 1B-SImethods).

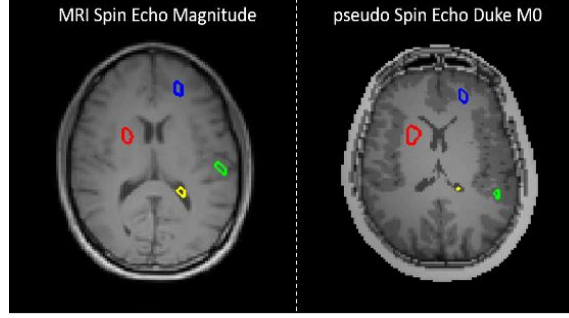


**Fig. 4B-SImethods:** Measured Spin Echo magnitude map (left) and pseudo Spin Echo map (right). The depicted four ROIs are used to compute the mean signal intensity values (see Tab. 1B-SImethods).

ROI color	Measured Spin Echo	Pseudo Spin Echo
Red	0.51	0.52
Blue	0.43	0.45
Green	0.39	0.36
Yellow	0.25	0.27

**Tab. 1B-SImethods:** Comparison between measured and pseudo Spin Echo magnitude values in the four ROIs depicted in Fig. 4B-SImethods. Spin Echo maps were normalized between 0 and 1.

### Part C: Choice of $cGAN_{\text{mask}}$

$\mathcal{L}_{cGAN}$ ,  $\mathcal{L}_{L1}$  and  $\mathcal{L}_{L2}$  are defined as:

$$\mathcal{L}_{cGAN} = \mathbb{E}_{x,y \sim p_{data}(x,y)} [\log D(x,y)] + \mathbb{E}_{x \sim p_{data}(x), z \sim p_z(z)} [\log (1 - D(x, G(x,z)))]$$

$$\mathcal{L}_{L1} = \mathbb{E}_{x,y \sim p_{data}(x,y), z \sim p_z(z)} [\|y - G(x,z)\|_1]$$

$$\mathcal{L}_{L2} = \mathbb{E}_{x,y \sim p_{data}(x,y), z \sim p_z(z)} [\|y - G(x,z)\|_2]$$

where  $x$  represent  $\{|\tilde{B}_1^+|, \tilde{\varphi}^+, mask\}$  or  $\{|\tilde{B}_1^+|, \tilde{\varphi}^+, pseudo\ MRI\}$  in the training set,  $y$  are the corresponding ground truth EPs maps and  $z$  is a vector drawn from the probability distribution  $p_z$  (28).

Different weights ( $\lambda_{GAN}$ ,  $\lambda_{L1}$ , and  $\lambda_{L2}$ ) were used during training. The phantom models 12 and 24, which were excluded from the training set, were used in the validation step to choose which combination of  $\lambda$ -weights had the lowest average normalized-root-mean-square error (NRMSE) computed over all the reconstructed EPs values for both phantoms. This combination of  $\lambda$ -weights was:  $\lambda_{GAN} = 2$ ,  $\lambda_{L1} = 100$ , and  $\lambda_{L2} = 200$  (Tab. 1C-SImethods). This combination was therefore used for testing using the phantom models 38, and 42, the phantom MRI measurements, the head model Duke M0 and the in-vivo MRI measurements. Of course, the phantom and head models, as well as the phantom and in-vivo MRI measurements used for the validation and the testing steps were excluded from the training dataset.

cGAN <sub>mask</sub> parameters			Reconstructed EPs using cGAN <sub>mask</sub>				Average NRMSE
			Phantom 12		Phantom 24		
$\lambda_{GAN}$	$\lambda_{L1}$	$\lambda_{L2}$	$\sigma$ [S/m]	$\epsilon_r$ [-]	$\sigma$ [S/m]	$\epsilon_r$ [-]	[%]
0	1000	2000	1.88 [0.02]	75.2 [2.1]	0.33 [0.07]	66.1 [1.1]	11.8
2	100	0	1.97 [0.02]	72.7 [2.5]	0.33 [0.02]	65.5 [0.4]	12.5
2	100	200	1.85 [0.02]	65.6 [2.4]	0.28 [0.02]	66.4 [0.4]	7.8
2	1000	0	1.90 [0.01]	73.5 [1.9]	0.30 [0.02]	65.4 [0.5]	9.9
2	1000	1000	1.95 [0.01]	71.4 [4.1]	0.28 [0.01]	64.1 [0.6]	9.7
2	1000	2000	1.86 [0.02]	74.6 [1.9]	0.33 [0.01]	72.1 [0.9]	14.4
<i>Reference EPs values</i>			<i>1.75 [-]</i>	<i>63 [-]</i>	<i>0.3 [-]</i>	<i>60 [-]</i>	

**Tab. 1C-SImethods:** The reconstructed mean EPs values and the standard deviations (between square brackets) are reported for the two phantoms used for the validation of the trained cGAN<sub>mask</sub>. The percentage of the average NRMSE computed over all the reconstructed EPs values for both phantoms is reported in the last column.

#### Part D: MR Sequences – Parameters

In the Tabs. 1D-SImethods and 2D-SImethods, the MR sequence parameters used for the AFI sequence and for the two Spin Echo sequences with opposite readout gradient polarities are reported. From the AFI sequence,  $\tilde{B}_1^+$  magnitude maps were obtained. From the Spin Echo sequences,  $\tilde{\varphi}^+$  maps were computed.

AFI	TR1	TR2	TE	Flip Angle	Field of View	Voxel size
Phantom	50 ms	250 ms	2.5 ms	65°	256×256×50 mm <sup>3</sup>	2×2×2 mm <sup>3</sup>
In-vivo	50 ms	250 ms	2.5 ms	65°	256×256×90 mm <sup>3</sup>	2×2×3 mm <sup>3</sup>

**Tab. 1D-SImethods:** Sequence parameters used for the AFI sequence. This sequence was adopted to map the magnitude of the transmit MR field.

Spin Echo	TR	TE	Field of View	Voxel size
Phantom	900 ms	5 ms	256×256×50 mm <sup>3</sup>	2×2×2 mm <sup>3</sup>
In-vivo	900 ms	5 ms	256×256×90 mm <sup>3</sup>	2×2×3 mm <sup>3</sup>

**Tab. 2D-SImethods:** Sequence parameters used for the two Spin Echo sequences performed with opposite readout gradient polarities to compensate for eddy-currents related artifacts. This sequence was adopted to map the transceive phase.

## SUPPORTING INFORMATION RESULTS

### Part A: Phantom EPs Reconstructions – Profiles and Absolute Errors

In the Fig. 1A-SI results below, the profiles of the reconstructed conductivity (a) and permittivity (b) maps for the phantom model 42 using MR-EPT (blue) and  $cGAN_{\text{mask}}$  (red) are shown. In black it is depicted the ground truth profile. These profiles were taken in direction left/right, as shown in the subfigures on the right (black lines). In these subfigures, the gray circles indicate for one slice the region of interest (ROI) used to compute the mean and standard deviation values of the reconstructed EPs values for the phantom models used for validation (phantom models 12, and 24) and for testing (phantom models 38, 42, and phantom MR measurements). The same ROI was used for all the other slices of the phantoms. In this way, errors arising from boundary regions in MR-EPT reconstructions were excluded.

In the Fig. 2A-SI results, the absolute error maps of conductivity and permittivity reconstructions are shown for the phantom model 42 and for the phantom MR measurements, which were both used for testing of the selected  $cGAN_{\text{mask}}$ . For the selected  $cGAN_{\text{mask}}$ , the absolute error for conductivity reconstructions is below 0.05 S/m (less than 10% relative error), both for the simulation and the MR measurement. The absolute error for permittivity reconstructions is below 5 for the simulated data, while it is a bit higher (about 8) for the reconstruction from the MR measurement. The higher error in permittivity reconstructions from MR measurements can be explained by intrinsic inaccuracies in the adopted  $\tilde{B}_1^+$  magnitude mapping technique. The absolute error for MR-EPT reconstruction from simulations is instead one order of magnitude higher than the error observed for the  $cGAN_{\text{mask}}$  reconstructions.

In Fig. 3A-SI results, reconstructed EPs maps and the mean  $\pm$  standard deviations values are reported for the phantom model 38, which was also used for testing. The relative errors for these reconstructions are in line with the relative errors previously observed for the phantom model 42.

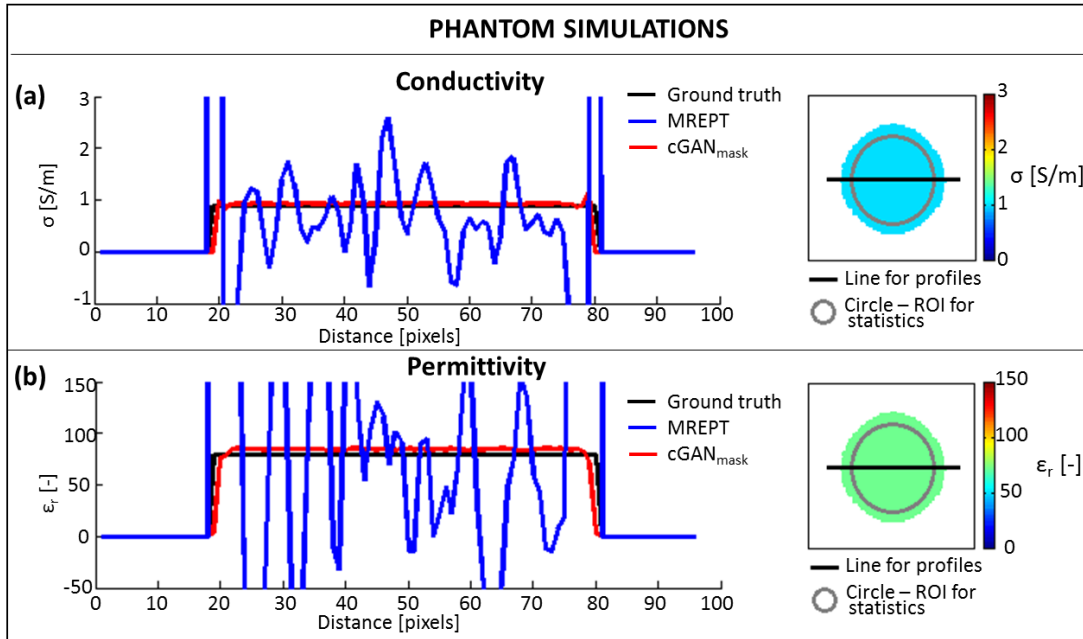


**Fig. 1A-SI results:** Phantom 42: profiles of the reconstructed EPs maps and definition of the region of interest used to compute mean and standard deviation values reported in the main manuscript. These profiles show how the  $cGAN_{\text{mask}}$  preserves boundaries better than MR-EPT reconstructions.



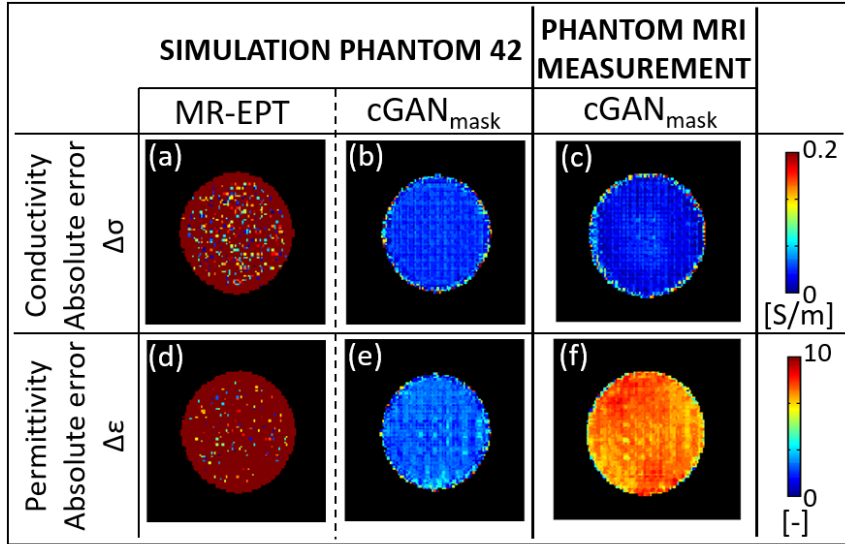


**Fig. 2A-SIresults:** Phantom model 42: absolute error maps for the reconstructed conductivity (a, b) and permittivity (d, e) maps using MR-EPT (a, d) and cGAN<sub>mask</sub> (b, e). Phantom MRI measurements: absolute error maps for the reconstructed conductivity (c) and permittivity (f) maps using cGAN<sub>mask</sub>.

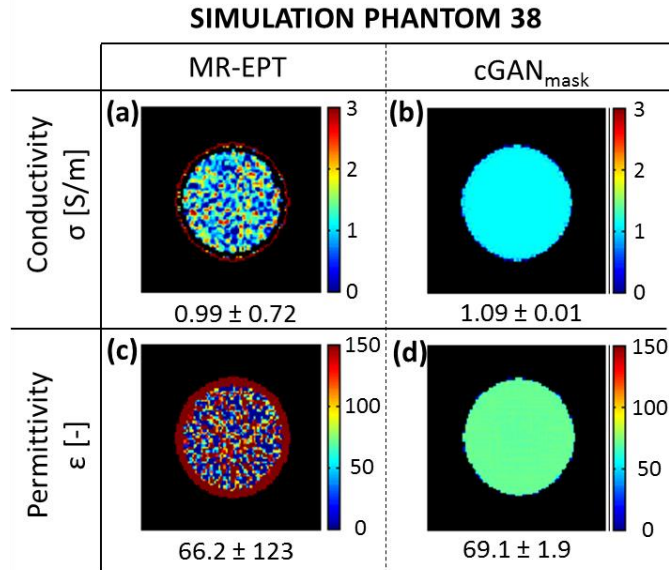


**Fig. 3A-SIresults:** Phantom 38 conductivity (a, b,) and permittivity (c, d,) maps reconstructed using MR-EPT (a, c,) and cGAN<sub>mask</sub> (b, d,). The reported numbers are the mean ± standard deviations values computed inside the region of interest indicated in the Fig. 1A-SIresults above. Ground truth EPs values are respectively  $\sigma = 1$  S/m and  $\epsilon_r = 66$  (see Supporting Information Methods).

### Part B: Head Model EPs Reconstructions – Absolute Errors

Finally, in Fig. 1B-SI results below, absolute error maps for conductivity and permittivity reconstructions for the head model Duke M0 are presented. From these maps, it can be observed the reduction of the absolute error at tissue boundaries if tissue information is given in input to the cGAN. Instead, the absolute error for MR-EPT reconstructions is at least one order of magnitude higher than the errors reported for the adopted cGANs.

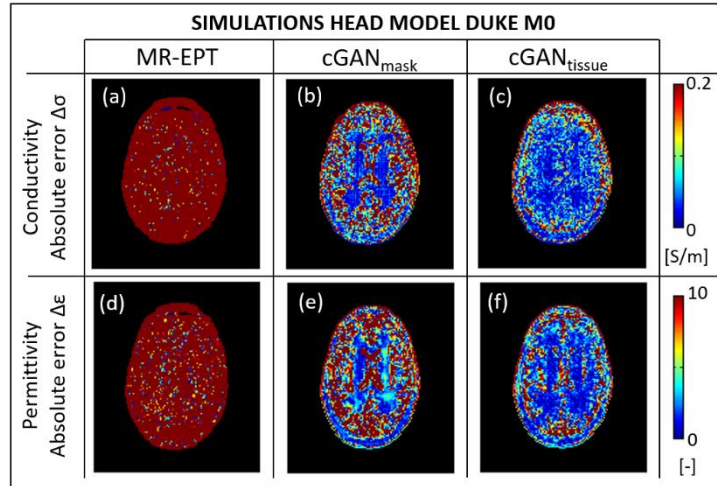


**Fig. 1B-SI results:** Head model Duke M0: absolute error for the reconstructed conductivity (a, b, and c) and permittivity (d, e, and f) maps using MR-EPT (a, d) and cGAN<sub>mask</sub> (b, e), and cGAN<sub>tissue</sub> (c, f).

## SUPPORTING INFORMATION DISCUSSION

### Part A: Impact of SNR

The impact of different SNR levels (no noise, 50, 20, and 5) on EPs reconstructions was investigated for the selected  $cGAN_{\text{mask}}$  ( $\lambda_{\text{GAN}} = 2$ ,  $\lambda_{\text{L1}} = 100$ , and  $\lambda_{\text{L2}} = 200$ ) using the testing head model Duke M0. From the Fig. 1A-SIdiscussion and the Tab. 1A-SIdiscussion below, it is visible that only for very low SNR levels (less than 20) EPs reconstructions are not accurate anymore. Typical SNR levels in MR experiments are higher than this value, thus suggesting that deep learning approaches would be sufficiently noise-robust for EPs reconstructions from MR measurements. Still, adequate knowledge on the SNR limits for DL-EPT reconstructions would be fundamental to allow for faster MR sequences with higher spatial resolutions (voxel size in the order of 1 mm) than typically employed MR sequences for EPs reconstructions.

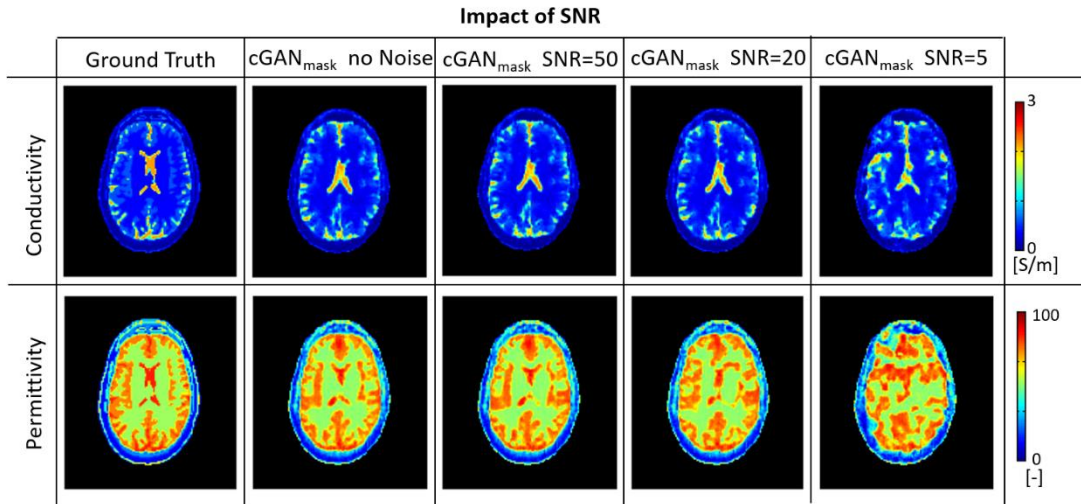


**Fig. 1A-SIdiscussion:**  $cGAN_{\text{mask}}$  EPs reconstructions for two different SNR levels.

SNR $_{ \vec{B}_1^+ }$	$\Delta\vec{\varphi}^+$	Impact of SNR					
		WM		GM		CSF	
		$\sigma$ [S/m] mean [std]	$\epsilon_r$ [-] mean [std]	$\sigma$ [S/m] mean [std]	$\epsilon_r$ [-] mean [std]	$\sigma$ [S/m] mean [std]	$\epsilon_r$ [-] mean [std]
No-noise	No-noise	0.38 [0.19]	54.9 [6.9]	0.65 [0.35]	71.9 [7.9]	1.77 [0.51]	83.1 [4.5]
50	0.02	0.38 [0.19]	55.1 [7.1]	0.65 [0.35]	71.7 [8.1]	1.77 [0.52]	82.9 [4.6]
20	0.05	0.38 [0.20]	56.1 [7.8]	0.65 [0.35]	71.3 [8.6]	1.76 [0.52]	82.2 [5.3]
5	0.2	0.44 [0.26]	62.5 [11.1]	0.67 [0.39]	68.9 [11.3]	1.58 [0.59]	78.7 [8.3]
<i>reference</i>		<i>0.34 [-]</i>	<i>52.6 [-]</i>	<i>0.59 [-]</i>	<i>73.4 [-]</i>	<i>2.14 [-]</i>	<i>84 [-]</i>

**Tab. 1A-SIdiscussion:** Mean and Standard deviation (inside square brackets) values of the reconstructed EPs in the WM, GM, and CSF tissues for the Head model Duke M0 using  $cGAN_{\text{mask}}$  and different SNR levels.

## Part B: Comparison U-Net and cGANs

To investigate the impact of different  $\lambda$ -weights on the reconstructed DL-EPT values of brain tissues, the average NRMSE was computed over the reconstructed EPs values in the WM, GM, and CSF tissues of Duke Model M0. For this evaluation, erosion of only 1 voxel was performed to exclude numerical errors at tissue boundaries that might arise from discretization and resizing of the simulated electromagnetic fields.

From Tab. 1B-SIdiscussion, it can be observed that the combination of  $\lambda$ -weights giving the lowest average NRMSE for  $cGAN_{\text{mask}}$  is:  $\lambda_{\text{GAN}} = 2$ ,  $\lambda_{\text{L1}} = 1000$ , and  $\lambda_{\text{L2}} = 2000$ . This  $cGAN_{\text{mask}}$  was used for DL-EPT reconstructions on the Duke model M0 with a tumor inclusion. It can also be observed that setting  $\lambda_{\text{GAN}} = 0$ , thus using a U-Net instead of a cGAN, could in principle lead to accurate results. For sake of completeness, in the below Fig. 1B-SIdiscussion, a comparison between EPs reconstructions for Duke M0 using the U-net, and the cGANs adopted in the manuscript is presented.

From Fig. 1B-SIdiscussion, it appears that EPs reconstructions using a U-Net are more blurred than cGAN reconstructions. However, we do not exclude that different training parameters could allow for more accurate results at tissue boundaries. This will be focus of future works.

cGAN <sub>mask</sub> parameters			Head Model Duke M0 EPs Reconstructions						Average NRMSE [%]
			WM		GM		CSF		
$\lambda_{\text{GAN}}$	$\lambda_{\text{L1}}$	$\lambda_{\text{L2}}$	$\sigma$ [S/m] mean [std]	$\epsilon_r$ [-] mean [std]	$\sigma$ [S/m] mean [std]	$\epsilon_r$ [-] mean [std]	$\sigma$ [S/m] mean [std]	$\epsilon_r$ [-] mean [std]	
0	1000	2000	0.35 [0.06]	55.2 [4.7]	0.62 [0.15]	73.3 [3.8]	2.06 [0.19]	83.2 [2.7]	11.8
2	100	0	0.41 [0.15]	55.6 [5.4]	0.67 [0.30]	71.8 [6.7]	1.90 [0.37]	82.9 [4.7]	24.8
2	100	200	0.38 [0.19]	54.9 [7.0]	0.65 [0.34]	71.9 [7.9]	1.77 [0.51]	83.0 [4.5]	29.4
2	1000	0	0.42 [0.15]	55.3 [6.5]	0.65 [0.30]	71.1 [6.9]	1.83 [0.47]	80.9 [4.9]	26.6
2	1000	1000	0.42 [0.17]	55.7 [6.4]	0.66 [0.34]	69.6 [6.0]	1.89 [0.44]	79.6 [5.8]	28.3
2	1000	2000	0.39 [0.14]	54.8 [5.7]	0.66 [0.30]	72.1 [6.7]	1.97 [0.33]	81.8 [3.9]	23.3

**Tab. 1B-SIdiscussion:**  $cGAN_{\text{mask}}$  EPs reconstructions in the WM, GM, CSF tissue for Duke M0, and the percentage of the average NRMSE among the reconstructed EPs values in these tissues for each combination of parameters  $\lambda_{\text{GAN}}$ ,  $\lambda_{\text{L1}}$ , and  $\lambda_{\text{L2}}$ .

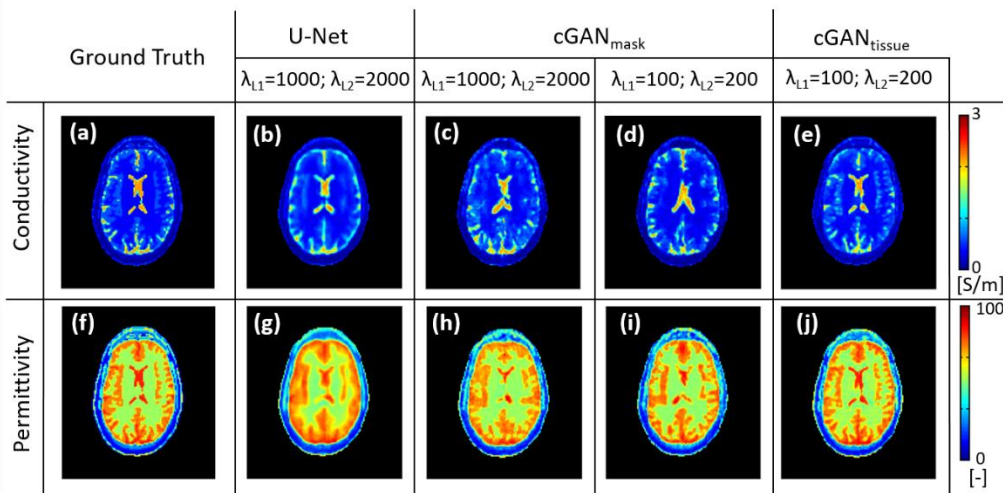


**Fig. 1B-SIdiscussion:** Comparison between EPs reconstructions using a U-Net (b, g), the  $cGAN_{\text{mask}}$  adopted for the tumor reconstruction (c, h), and the  $cGAN_{\text{mask}}$  (d, i) and  $cGAN_{\text{tissue}}$  (e, j) adopted for DL-EPT reconstructions in the manuscript.